ADVANCED OPTICAL MATERIALS
www.advopticalmat.de

A Novel Multi-Functional Thiophene-Based Organic Cation as Passivation, Crystalline Orientation, and Organic Spacer Agent for Low-Dimensional 3D/1D Perovskite Solar Cells

*Ali Semerci, Ali Buyruk, Saim Emin, Rik Hooijer, Daniela Kovacheva, Peter Mayer, Manuel A. Reus, Dominic Blätte, Marcella Günther, Nicolai F. Hartmann, Soroush Lotfi, Jan P. Hofmann, Peter Müller-Buschbaum, Thomas Bein, and Tayebeh Ameri**

Recently, the mixed-dimensional (3D/2D or 3D/1D) perovskite solar cells using small organic spacers have attracted interest due to their outstanding long-term stability. Here, a new type of thiophene-based organic cation 2-(thiophene-2yl-)pyridine-1-ium iodide (ThPyI), which is used to fabricate mixed-dimensional 3D/1D perovskite solar cells, is presented. The ThPyI-based 1D perovskitoid is applied as a passivator on top of a 3D methyl ammonium lead iodide (MAPI) to fabricate surface-passivated 3D/1D perovskite films or added alone into the 3D perovskite precursor to generate bulk-passivated 3D MAPI. The 1D perovskitoid acts as a passivating agent at the grain boundaries of surface-passivated 3D/1D, which improves the power conversion efficiency (PCE) of the solar cells. Grazing incidence wide-angle X-ray scattering (GIWAXS) studies confirm that ThPyI triggers the preferential orientation of the bulk MAPI slabs, which is essential to enhance charge transport. Champion bulk-passivated 3D and surface-passivated 3D/1D devices yield 14.10% and 19.60% PCE, respectively. The bulk-passivated 3D offers favorable stability, with 84% PCE retained after 2000 h without encapsulation. This study brings a new perspective to the design of organic spacers having a different binding motif and a passivation strategy to mitigate the impact of defects in hybrid 3D/1D perovskite solar cells.

1. Introduction

During the last decade, 3D organic–inorganic halide perovskites (OIHPs) have emerged as promising absorber materials for photovoltaic applications due to their superior properties such as high absorption coefficient, long diffusion length of the charge carriers, fast charge transport, and tunable bandgap. The 3D OIHPs have demonstrated rapid increase in power conversion efficiency (PCE) from 3.8% to 25.2%.[1–9] On the other hand, their moderate intrinsic stability against moisture and heat still has been a concern with a view on possible commercialization.[10–14] Instability of the 3D methyl ammonium lead iodide (MAPI) perovskite is assumed to be due to its crystalline structure. Ionic migration is now well recognized to affect the photovoltaic properties of perovskite solar cells. Especially, the ionic migration causes the generation and displacement of vacancies in perovskite materials. OIHPs are mixed ionic–electronic conductors with iodide ions as the majority of ionic carriers.

A. Semerci, A. Buyruk, R. Hooijer, P. Mayer, D. Blätte, M. Günther, T. Bein, T. Ameri
Department of Chemistry and Center for NanoScience (CeNS)
Ludwig-Maximilians-Universität München
Butenandtstrasse 5–13 (E), 81377 Munich, Germany
E-mail: tayebeh.ameri@ed.ac.uk

S. Emin
Materials Research Laboratory
University of Nova Gorica
Vipavska 13c, Ajdovščina 5270, Slovenia

The ORCID identification number(s) for the author(s) of this article can be found under https://doi.org/10.1002/adom.202300267

DOI: 10.1002/adom.202300267

D. Kovacheva
Institute of General and Inorganic Chemistry
Bulgarian Academy of Sciences
Sofia 1113, Bulgaria

M. A. Reus, P. Müller-Buschbaum
TUM School of Natural Sciences
Department of Physics
Chair for Functional Materials
Technical University of Munich
James-Franck-Str. 1, 85748 Garching, Germany

N. F. Hartmann
Attocube systems AG
Nanoscale Analytics
neaspec
Eglfinger Weg 2, 85540 Haar, Germany

S. Lotfi, J. P. Hofmann
Surface Science Laboratory
Department of Materials and Earth Sciences
Technical University of Darmstadt
Otto-Berndt-Str. 3, 64287 Darmstadt, Germany

The diffusion coefficient of 10−12 cm2 s−1 for I− ions is several orders of magnitude higher than the value of 10−16 cm2 s−1 for CH3NH3+. The organic cations such as CH3NH3+or NH2CH = NH2+ show however moderate degrees of freedom for ion migration, which is one of the main reasons why 3D perovskite structures have poor stability.[15–17] Adsorption of water and oxygen molecules at vacancy sites is predominant than at pristine surfaces accelerating perovskite degradation via the vacancy-assisted mechanism. When MAPI is exposed to water, it degrades to lead(II)iodide (PbI2), iodide anions, and methylammonium cations (MA+).[16,17] In addition to the instability issues, surface and bulk defects in 3D polycrystalline perovskites can strongly affect the carrier recombination and hence performance of solar cells.

In the meantime, lower-dimensional relatives of the 3D halide perovskites have attracted growing attention. Here, layers of larger organic cations separate slabs of octahedral perovskite-like inorganic layers, with profound impact on band structure, charge carrier transport, and often much improved stability.[14] However, the insulating nature of organic spacers in the low-dimensional perovskite can limit the conductivity and can contribute to low photovoltaic performance despite their enhanced environmental stability.[18]

To address the above-mentioned challenges, a strong research focus has been put on developing new strategies and approaches to suppress recombination processes and overcome the stability issues of 3D halide perovskite structures.[19,20] Among the various passivating additives, it has been reported that ammonium salts can effectively diminish the impact of defects caused by dangling bonds or vacancies.[21,22] Another strategy for passivation is the introduction of low-dimensional perovskites in the 3D perovskite system.[23] Following this approach, the passivation of defects can be achieved, and the intrinsic stability issues of the 3D MAPI structure can be addressed. Therefore, passivated and mixed-dimensional perovskite solar cells (PSCs) have been fabricated using small organic molecular spacers.[24] The low-dimensional (1D or 2D) perovskite structures found in the resulting mixed-dimensional perovskites serve both as passivating agents to reduce the impact of defects and as heterojunctions that enhance the fluorescence lifetimes in the perovskite structure.[21] Hence, mixed-dimensional perovskites recently evolved as suitable photovoltaic (PV) candidates due to their encouraging environmental stability and wide tunability of optical properties.[25–30] Here, the higher perovskite stability could be attributed to the hydrophobic nature of the organic spacers used.[31,32] For example, 1D perovskitoids can be used both on top of 3D perovskite films or in the bulk perovskite by adding the desired organic cations to the precursor solution to improve efficiency and stability of perovskite PV devices.[33–35]

P. Müller-Buschbaum
Heinz Maier-Leibnitz-Zentrum (MLZ)
Technical University of Munich
Lichtenbergstr. 1, 85748 Garching, Germany

T. Ameri
Institute for Materials and Processes, Chemical Engineering
University of Edinburgh
Sanderson Building, Robert Stevenson Road, Edinburgh, Scotland EH9 3FB, United Kingdom

It has been demonstrated that the metal halide bonds can break upon illumination, followed by rearrangement of the perovskite crystal structure.[30] The individual metal halide octahedra formed during this reorganization are more stable than the regularly bonded ones.[36] In 1D perovskitoid structures, the $[PbI_6]^{4-}$ octahedral framework structure based on edge, face, or corner-sharing connect to the organic spacers. In this case, the metal halide octahedra are surrounded by organic spacer molecules.[37] Among the reasons for the instability of tin and lead based perovskites are the high-energy orbitals ($5s^2$ (Sn^{2+})/$6s^2$ (Pb^{2+})) near the top of the valance band, which are more reactive.[38] The edge or face-sharing binding motif of 1D structures stabilizes these high-energy orbitals, which leads to better environmental stability.[39] For example, Liu et al. employed 1D PbI_2-bipyridine to incorporate into the 3D MAPI perovskite structure. Thereby, the obtained 1D perovskite layers reduced the ion migration by improving the stability of the 3D/1D perovskite structure.[40] Gao et al. used thiazole ammonium iodide to form a 1D $TAPbI_3$ capping layer on 3D MAPI, improving the stability and performance of corresponding PSCs compared to the 3D MAPI control device.[39] Yang et al. used polymerizable propargylammonium to fabricate 1D structures at the surface and grain boundaries in a mixed-dimensional 3D/1D perovskite. By this means, they enhanced the charge transport and decreased the tensile strain of perovskite layers.[34]

Solar cells with grain boundary passivation have been reported to be superior in performance compared to those without passivation since grain boundaries can act as recombination centers. The most studied defects in MAPI perovskites are the point defects. Twelve different types of defects are generally observed in MAPI, including vacancies, interstitials, and anti-site occupations.[41] Defects at grain boundaries in polycrystalline perovskites are a major source for recombination of photo-generated carriers. Typical examples of tailored passivation schemes of defects include the use of polymers, quaternary ammonium salts, and other organic compounds.[42–50] In order to reduce non-radiative recombination in the bulk and at grain boundaries, both inorganic additives (Cl^-, SCN^-, etc.) or organic molecules have been introduced into the perovskite materials.[51]

In this work, a novel organic spacer 2-(thiophene-2yl-) pyridine-1-ium iodide (ThPyI) was developed to fabricate mixed-dimensional bulk-passivated 3D and surface-passivated 3D/1D perovskite solar cells. The ThPyI organic spacer is proposed to generate 1D structures at the grain boundaries of surface-passivated 3D perovskite films. Further, the ThPyI organic spacer is also viewed as a promising passivating agent for reducing other defects in the 3D MAPI and as a suitable material to create 3D/1D heterostructure perovskites for efficient charge separation. Employing the two different passivation methods of bulk and surface treatment, the impact of this organic spacer on the photovoltaic performance, stability, structural, as well as optoelectronic properties of the corresponding perovskite solar cells was investigated. The optimized PCE of bulk-passivated 3D and surface passivated 3D/1D mixed-dimensional PSCs reached 14.10% and 19.60%, respectively, with significantly improved stability compared to the reference 3D PSCs.

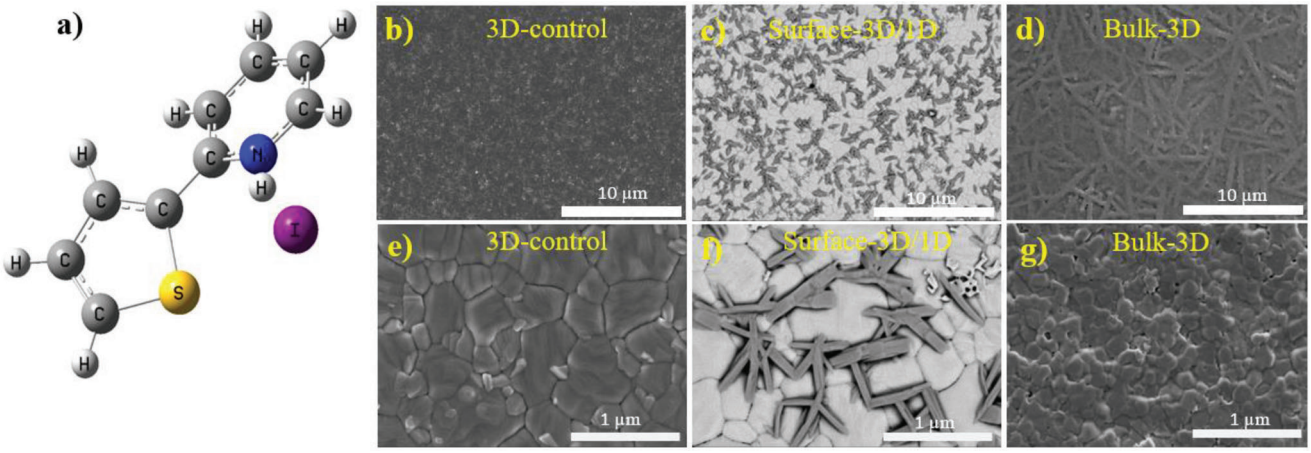

Figure 1. a) Molecular structure of ThPyI spacer. SEM images of b,e) 3D MAPI control film, c,f) surface-passivated 3D/1D, and d,g) bulk-passivated 3D MAPI perovskite film.

2. Results and Discussion

The molecular structure of the ThPyI organic spacer used in this work is illustrated in **Figure 1**a. The characterization of ThPyI was performed with nuclear magnetic resonance (^{1}H-,^{13}C-NMR) and mass spectroscopy (Figure S1a–d, Supporting Information). The so-called surface-passivated 3D/1D device was prepared by spin-coating of ThPyI on top of MAPI films.

As for the bulk-passivated 3D perovskite, the fabrication process is similar to the case of MAPI, with the addition of ThPyI into the precursor solution. The latter sample comprising both ThPyI and methylammonium chloride (MACl) agents is called "bulk-passivated 3D" from here on. For the purpose of comparison with the bulk-passivated 3D perovskite, MAPI-based control devices were fabricated with and without MACl additive. It is worthwhile mentioning that based on a known effect, MACl is added to the bulk-passivated 3D MAPI to achieve preferential orientation of the crystal grains.[34] However, in the surface-passivated samples, the use of MACl was avoided due to the use of excess PbI_2 (5% mol) in the precursor solution. Further processing details are provided in the Experimental Section. Interestingly, both methods of ThPyI-based surface and bulk passivation result in the formation of a new perovskite-related phase, which is identified as the 1D perovskitoid structure ($C_{18}H_{16}I_8N_2Pb_3S_2$), as explained in the following.

To evaluate the morphology of 3D control, bulk-passivated 3D, and surface-passivated 3D/1D MAPI perovskite films, scanning electron microscopy (SEM) measurements were performed. As shown in the top-view SEM images of the corresponding films in Figure 1b–g, the active MAPI layers completely cover the substrate surface. The grain-based morphology in the 3D control and the surface-passivated 3D/1D films looks very similar. However, on the surface-passivated 3D/1D perovskite film, needle-like new features form preferentially at the 3D perovskite grain boundaries as shown in Figure 1c. These needles assemble into an interconnected network which may affect the charge transport across the grains. In comparison to the 3D MAPI control, bulk-passivated 3D MAPI perovskite film shows a different surface morphology. In the 3D control with MACl, the interconnected needles were no longer observable (Figure S2, Supporting Information).

The grains of bulk-passivated 3D perovskite seem to be more closely connected (or fused) which appears to obscure their grain boundaries. At lower magnification (×2000) the bulk-passivated 3D perovskite shows interconnected needle-shape formations as shown in Figure 1d. It is well-known that needle-like morphology can offer enhanced charge collection compared to pure planar films.[52–54] Here, the bulk-passivated 3D film shows homogenous composition without any formations assigned to an additional phase.

X-ray diffraction (XRD) measurements were employed to investigate the crystallinity of a 1D single crystal, 3D control, surface-passivated 3D/1D, and bulk-passivated 3D perovskite films as shown in **Figure 2**a. The main XRD peaks of the 3D control appear at 14.19° and 28.50° 2θ, which correspond to (110) and (220) planes, respectively. As illustrated in the XRD data, the bulk-passivated 3D perovskite film (3D Bulk with MACl) fabricated using MACl also exhibits these two dominant diffraction peaks. The lack of additional reflections or any peak shift indicates that the addition of the ThPyI organic spacer into the 3D perovskite film does not change the MAPI lattice. The absence of other diffraction peaks from MAPI or a possible second phase (including below <12° 2θ) confirms both the phase purity and the preferential orientation of the MAPI grains. Here, the preferential orientation is achieved by the addition of MACl, which is widely used in the literature as an additive to boost the PCE.[55]

As observed in the XRD pattern of the surface-passivated perovskite, a new peak appears at low 2θ values (7.54°). This additional peak can be related to the needle-like formations at the 3D perovskite grain boundaries shown in Figure 2b. Moreover, this new phase did not result from PbI_2 or from the pure ThPyI organic spacer according to the XRD patterns. To elucidate the structure of the needle-like formations on the surface-passivated perovskite film, single crystals were grown by reacting stoichiometric ratios of PbI_2 and ThPyI (Figure S3, Supporting Information). The structural analysis of the needle-shaped single crystals was performed using both powder XRD data shown in Figure 2

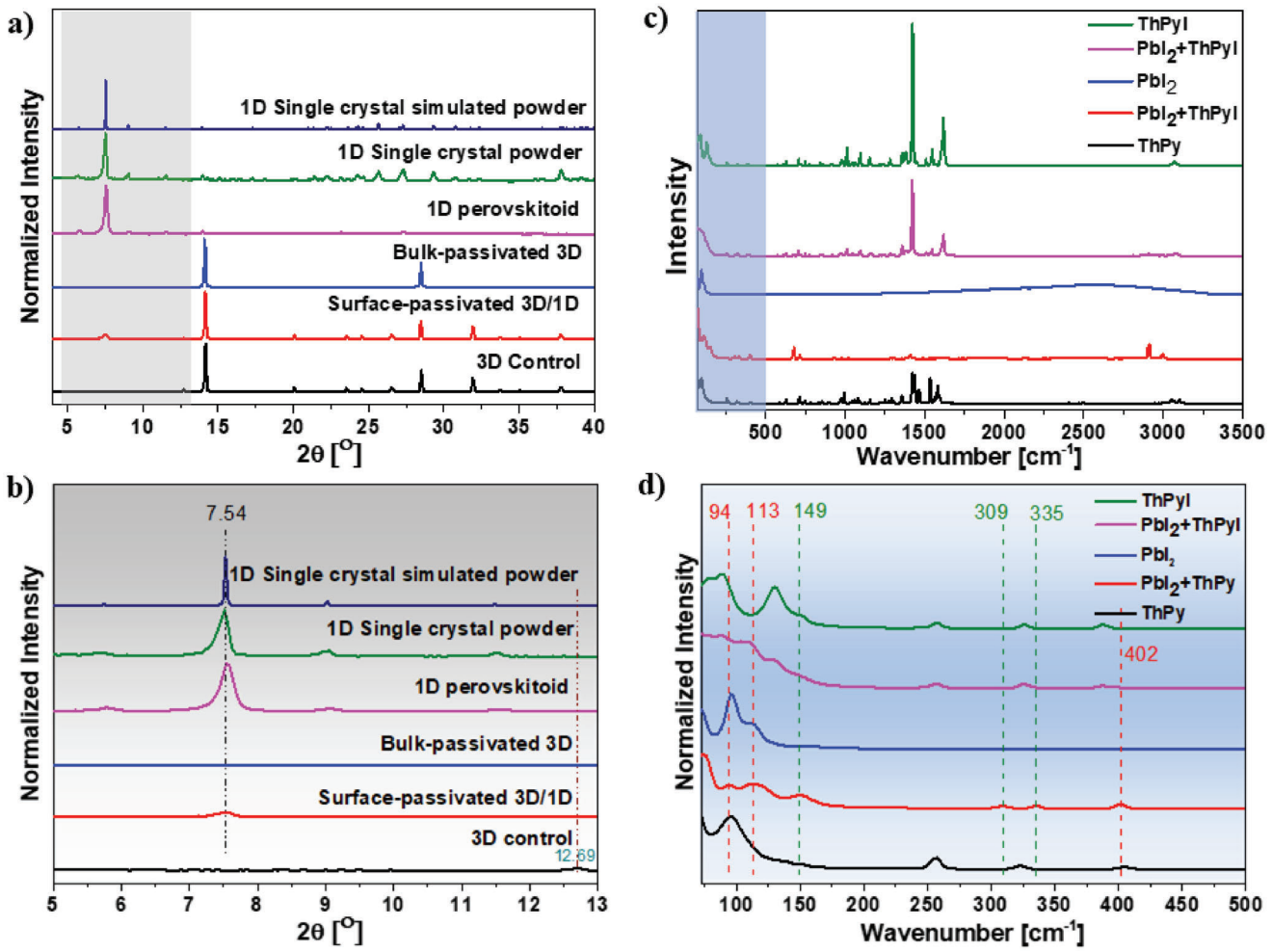

Figure 2. XRD patterns of pure 1D perovskitoid film and 1D single crystal powder, simulated 1D, 3D control, bulk-passivated 3D, and surface-passivated 3D/1D perovskite thin films showing a) wide scan and b) enlarged XRD pattern from 5°and 13° 2θ. c) Raman spectra of powder forms taken of the ThPy ligand, ThPyI, PbI_2, the mixture of PbI_2 + ThPy, and the mixture of PbI_2 + ThPyI. d) Narrow range Raman spectra taken from (c).

and single crystal diffraction (Figure S4, Supporting Information).

To further confirm the presence of both the 3D control MAPI and the 1D perovskitoid, powder XRD measurements, and Rietveld refinements were carried out. The results of the Rietveld refinement of the structure and the Rietveld plot of the fit are presented (Figures S5,S6 and Table S2, Supporting Information). The whole powder pattern fitting procedure of the 1D-film (Figure S6, Supporting Information) revealed a single phase 1D perovskitoid with unit cell parameters a = 25.494(4) Å, b = 61.82(1) Å and c = 4.5968(8) Å, which are close to those observed for the single crystal phase (Table S1, Supporting Information).

According to the single crystal diffraction results and the calculated powder diffraction pattern, the single crystal data perfectly matches the XRD pattern of the 1D perovskitoid structure {with reflections at 5.7° (040), 7.5° (220), 9.0° (240), 11.0° (260), and 11.4° (080)} The crystal structure of the 1D perovskitoid corresponds to the unit cell formula $C_{18}H_{16}I_8N_2Pb_3S_2$ given in **Figure 3**. In the crystal structure, three edge-shared octahedra are accompanied by two edge-to-edge aligned organic spacer (ThPyI) molecules, which engage in strong N^+-H···I–Pb hydrogen-bonding interactions (Figure S4, Supporting Information). According to the obtained crystallographic data, the 1D perovskitoid features an orthorhombic crystal system (*Fdd*2 space group) (Table S1, Supporting Information). In good agreement with the single crystal XRD data of the 1D perovskitoid, the new peak emerging at 7.54° for the surface-passivated sample can be assigned to the 1D perovskitoid phase as shown in Figure 2b. We note that under these conditions, reflections corresponding to the 1D phase are missing in the diffractogram of bulk-passivated 3D MAPI. However, when the passivation is done without (wo) added MACl, the dominant peak at 7.54° is clearly seen, which indicates the formation of the 1D perovskitoid phase (Figure S7, Supporting Information).

To gain additional insight about the needles formed on the surface of the 3D/1D perovskite film, Raman spectroscopy was employed as shown in Figure 2c,d.

The Raman spectra of the ThPyI organic spacer, its neutral form (ThPy, unprotonated), PbI_2, and mixtures of PbI_2 + ThPy, and PbI_2 + ThPyI were compared to eliminate the possibility

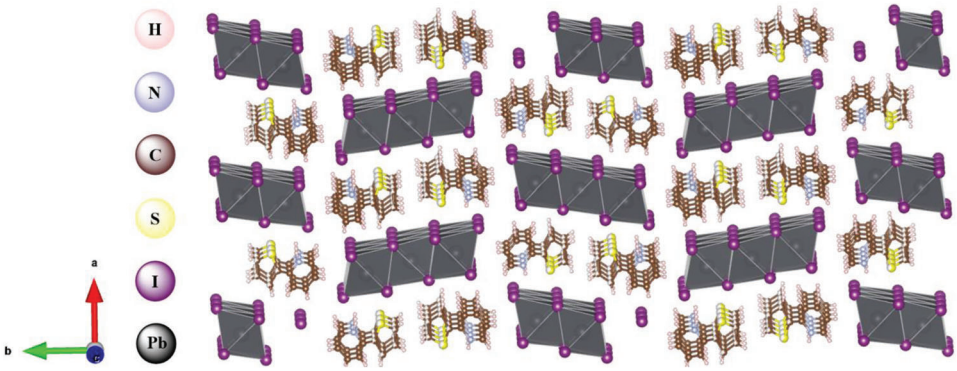

Figure 3. Schematic representation of the crystal structure of the 1D perovskitoid unit cell. The free iodine atoms which appear in the schematic are part of the octahedra of the adjacent unit cell which is not involved here.

that the needles derive from a basic complex form of PbI_2 with the organic spacer (Figure S8, Supporting Information).[56] The Raman vibrational frequencies of the mixture of PbI_2 + ThPy appear at 74, 94, 112, 149, 309, 335, and 402 cm^{-1} (red and green dashed lines in Figure 2d). Some of these signals (red dashed lines) are shifted compared to those of PbI_2 and ThPy. Moreover, two Raman vibrational frequencies of free ThPy at 258 and 323 cm^{-1} disappear, while two new vibrational frequencies appear at 309 and 335 cm^{-1} (green dashed lines). These new signals are in the region of the metal-nitrogen stretching vibrations (200–600 cm^{-1}). In sum, these observations suggest that a new phase has formed via a chemical reaction between PbI_2 and ThPy.[57]

Unlike the mixture of PbI_2 + ThPy, the Raman spectrum of the mixture of PbI_2 + ThPyI shows no shifts and/or new signals. This indicates that here the Raman signals are due to the unreacted mixture of PbI_2 and ThPyI since these overlap with the signals of pure PbI_2 and ThPyI. To support the Raman results for the unreacted PbI_2 + ThPyI mixture, its solution-state ^{1}H-NMR was evaluated (Figure S1d,e, Supporting Information). In the PbI_2–ThPyI solution, no new ^{1}H-NMR signal associated with a chemical reaction was recorded. Interestingly, the signal of the proton (N^+-H) of the pyridine group shows an up-field shift (shielding effect), which is a specific hint as to the strong N^+-H···I-Pb–I hydrogen-bonding interactions. In addition to the up-field shifted proton (N^+-H), obvious up-field shifts for the neighboring protons of both rings (ThPy) are also observed. Together, these results confirm that complexation between ThPyI and PbI_2 is not the cause of the needle-like formations after surface treatment.

To study the needle-like formations on the surface-passivated 3D/1D perovskite sample at the nanoscale (10–20 nm spatial resolution), nano-FTIR spectroscopy was used.[58]

Two locations were identified from the broadband near-field amplitude image taken on the surface-passivated 3D/1D sample, presented in **Figure 4**a. While spot (A) was taken on the top of a 3D perovskite grain, spot (B) was recorded from the needle-like formations (1D phase) which is observed in SEM images (Figure 1c–f). The selected broadband infrared range for these two spots varied from 1100 to 1900 cm^{-1} as given in Figure 4b. In spot B the intense vibration at 1471 cm^{-1} (orange highlight) was assigned to the well-known symmetric NH_3^+ bending of methylammonium in MAPI.[59] Additionally, four new signals (highlighted in green) were observed for position B corresponding to the needle-like formation, which are not seen in the MAPI grain (position A).[60] Furthermore, these new signals are similar but slightly shifted to lower wavenumbers compared to those seen in the ThPyI organic spacer (Figure S9, Supporting Information). The new vibrations can be assigned to the 1D perovskitoid phase. The observed shift to lower wavenumbers in the 1D perovskitoid is attributed to the local environment in the 1D perovskitoid crystal structure. To probe the distribution of the 1D formations in detail, position-dependent measurements (one spectrum at every 30 nm) along a 1.2 µm sample distance were carried out as indicated by the orange dashed arrow in Figure 4c. We note that the signals from the 1D phase formations are predominantly observed at the 3D perovskite grain boundaries as shown in Figure 4c,d.

Grazing incidence wide-angle X-ray scattering (GIWAXS) was conducted to evaluate the orientation of perovskite crystallites in the 3D control, bulk-passivated 3D MAPI, and surface-passivated 3D/1D perovskite films with and without MACl respectively. The 3D reference crystallizes with random orientation, observable through the diffraction rings as shown in **Figure 5**a. This result is in accordance with previous studies.[61] The reflection along the azimuthal angle around 0°, below the first diffraction ring corresponding to MAPI, corresponds to the (001) plane of PbI_2. Excess PbI_2 is common for untreated 3D MAPI thin films and is caused by surface degradation of the perovskite film, as well as by the excess use of PbI_2 in the precursor solution.[62]

The 3D reference with MACl displays the same features, although the intensity of the PbI_2 reflection is increased and the MAPI diffraction rings show a slight (110) horizontal orientation (orientation always with regard to the substrate plane), as shown in Figure 5d. The surface-passivated 3D/1D samples display a new set of reflections in the lower q region, shown in Figure 5b. These reflections appear with a horizontal orientation and can be assigned to the (040), (220), and (240) reflections of the 1D perovskitoid phase. The surface-passivated 3D/1D samples with MACl do not show any preferential orientation, or any diffraction corresponding to the 1D perovskitoid phase, see Figure 5c. The bulk-passivated 3D MAPI without MACl samples display oriented reflections for the 3D MAPI phase, indexed and shown in Figure 5e, as well as the reflections of the 1D perovskitoid phase with a horizontal orientation.

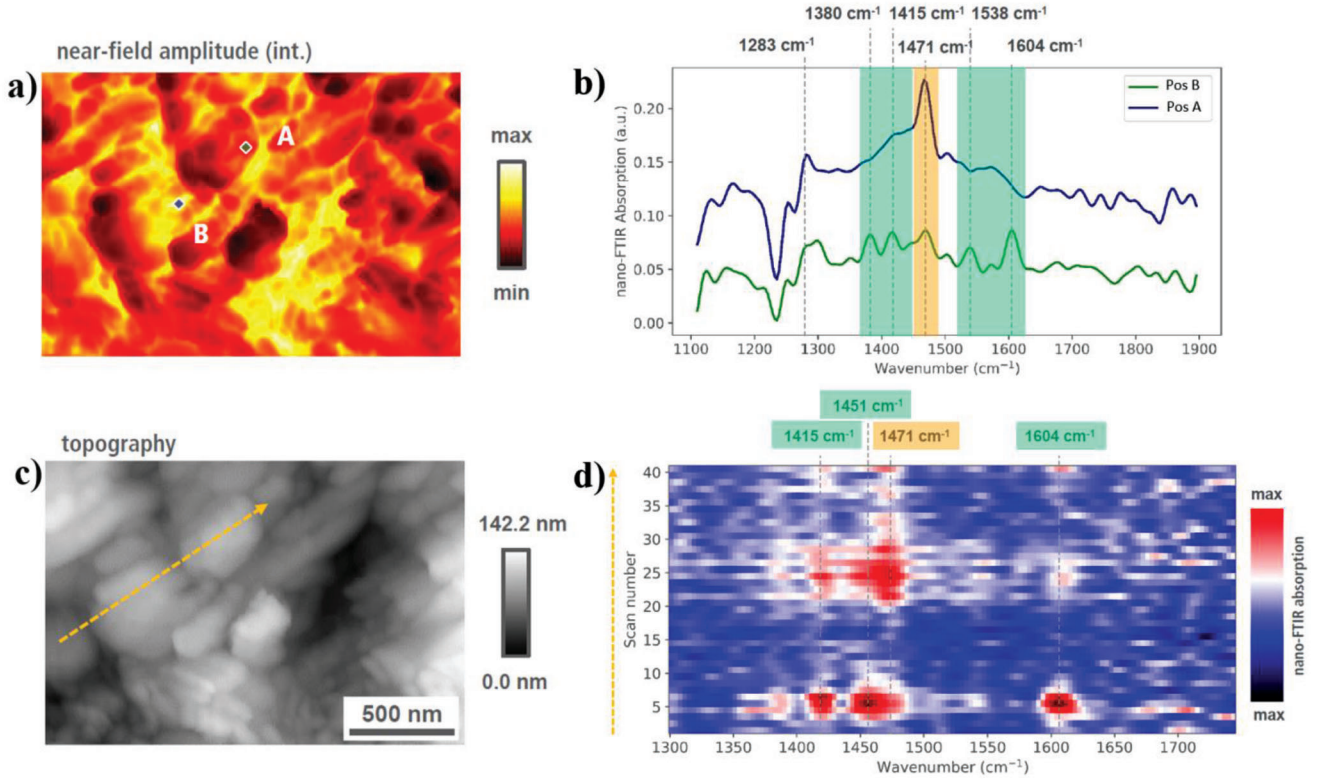

Figure 4. Nano-FTIR analysis of surface-passivated 3D/1D perovskite film. a) Broadband, integrated near-field amplitude image, b) spectra recorded from the positions in A and B shown in (a), c) topography of the surface, and d) spectral image recorded from the line scan in (c).

These GIWAXS results are consistent with the XRD results where the 1D perovskitoid phase can be clearly seen in the bulk-passivated 3D film MAPI without MACl (Figure S7a, Supporting information). Last, the bulk passivated 3D MAPI with MACl displays a different orientation for the MAPI reflections and only a very weak reflection of the (220) plane corresponding to the 1D perovskitoid phase. For both bulk-passivated 3D MAPI samples, the ThPyI spacer has a strong influence on the orientation of the MAPI film, while the (110) planes reorient from horizontal to vertical orientation with respect to the substrate if MACl is additionally employed to control the crystallization. The absence of any strong diffraction, corresponding to the 1D phase in the bulk-passivated 3D MAPI with MACl sample in Figure 5f, (Figure S7a, Supporting Information), points toward an interaction between MACl and ThPyI in the crystallization process. The additional MA^+ in the crystallization competes with the amount of Pb^{2+} ions, which is the same for both thin films, that is, the same amount of PbI_2 in the precursor solution. This is also evident in the surface passivated 3D/1D samples, where if MACl is used in combination with the ThPyI spacer no 1D phase is observed, but rather a complete consumption of the excessive PbI_2 into MAPI as shown in Figure 5c.

In conclusion for the surface-passivated 3D/1D samples, the combination of the data from the SEM, nano FTIR, and GIWAXS confirm the formation of the 1D phase at the surface and grain boundaries of the perovskite thin film. The ThPyI bulk passivated sample shows evidence of the 1D phase formation in addition to a pronounced horizontal orientation of (110) planes of the 3D MAPI perovskite phase. However, when MACl is used as a co-additive in the bulk-passivated sample, the 3D MAPI perovskite orientation is changed toward vertical (110) orientation and the diffraction peaks of the 1D phase are missing or have a noticeable intensity attenuation. At this stage, it is not clear if the ThPyI spacer in the presence of MACl forms an amorphous 1D phase or if it prefers to stay in amorphous molecular (pure ThPyI) form. The impact of the ThPyI and MACl agents on the morphology of surface-passivated and bulk-passivated perovskite films is schematically illustrated in **Figure 6**a–f. To further elucidate the structural properties of the bulk passivated 3D MAPI samples (without MACl), high-resolution transmission electron microscopy (HR-TEM) studies were carried out as shown in Figure 5g,h.

The HR-TEM images from selected locations confirm the existence of different lattice spacings. The calculated *d*-spacings corresponding to these planes are summarized (Table S3, Supporting Information). The narrow interplanar lattice spacing of 2.87 Å corresponds to the (231) diffraction peak of the 3D MAPI phase in Figure 5g.

On the other hand, the lattice spacings of 7.70 and 11.74 Å match the (080) and (220) planes of the 1D perovskitoid, respectively, as shown in Figure 5g,h. Overall, the interplanar lattice distances agree with the corresponding XRD data (Table S4, Supporting Information). The HR-TEM results demonstrate that the 1D perovskitoid phase distributes in the 3D perovskite phase. TEM images were also recorded from bulk-passivated 3D MAPI prepared using MACl. In this case, we observed

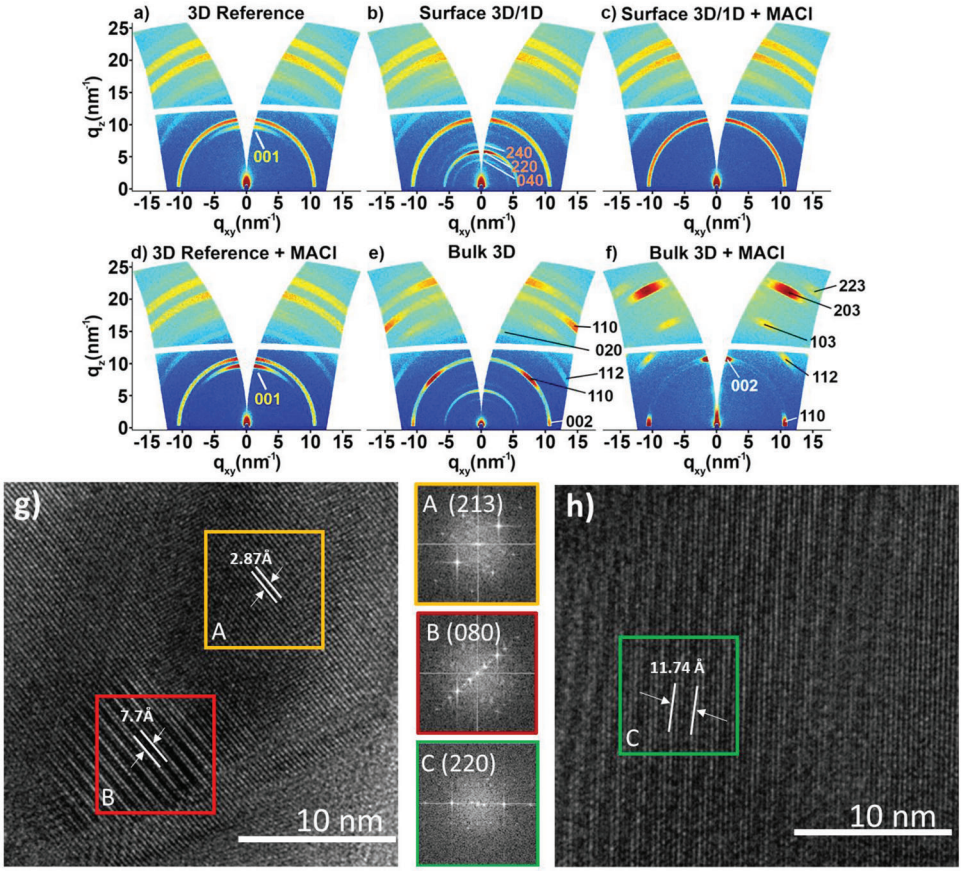

Figure 5. GIWAXS data of a) 3D control MAPI (with +5% excess PbI_2), b) surface-passivated 3D/1D without MACl, c) surface-passivated 3D/1D with MACl, d) 3D control MAPI of the bulk-passivated sample with MACl, e) bulk-passivated 3D MAPI without MACl, and f) bulk-passivated 3D MAPI with MACl. g,h) TEM images of bulk-passivated 3D MAPI (without MACl) perovskite film and corresponding fast Fourier transforms (FFT) taken from the marked areas in A, B, and C.

nanoscopic objects like nanorods which after recrystallization under the intensive electron beam yielded crystallites (of unknown structure) with lattice spacing equal to 7.70 Å (Figure S10, Supporting Information).

UV-vis absorption spectroscopy was employed to investigate the optoelectronic characteristics of the perovskite films (Figure S11a, Supporting Information). In comparison with the 3D MAPI control film, surface-passivated 3D/1D films (thickness of about 600 nm) show no significant changes, implying that the 1D perovskitoid on top of the 3D structure does not significantly change the absorption features of the photoactive film. However, the bulk-passivated 3D film exhibits a weaker absorption while retaining the spectral features of MAPI. This is attributed to the different thicknesses of the bulk-passivated 3D film (thickness of about 400 nm).

In line with the similar optical absorption spectrum, the surface-passivated 3D/1D hybrid device shows an External Quantum Efficiency (EQE) response similar to the 3D MAPI control (Figure S12a, Supporting Information). In the case of the bulk-passivated 3D MAPI sample, the EQE is higher than that of the corresponding 3D MAPI reference with MACl (Figure S12b, Supporting Information). To determine the energy levels of the bulk-passivated 3D MAPI phase, ultraviolet photoelectron spectroscopy (UPS) was employed (Figure S11b, Supporting Information). The valence band maximum (VB) and conduction band minimum (CB) of the bulk-passivated 3D perovskite are estimated at −5.81 and −4.21 eV, respectively, which are very close to the values of 3D MAPI (Figure S11c, Supporting Information). These energy levels are also compatible with the hole transport layer comprising poly(3,4-ethylenedioxythiophene) poly(styrenesulfonate) (PEDOT:PSS), (−5.1 eV; VB) and the electron transport layer comprising phenyl-C_{61}-butyric acid methyl ester($PC_{61}BM$), (−3.8 eV; VB).

Steady-state photoluminescence (SSPL) and time-resolved photoluminescence decay (TRPL) measurements were carried out to unravel the charge recombination processes in the 3D MAPI control, bulk-passivated 3D, and surface-passivated 3D/1D films as shown in **Figure 7**a–d. In the case of the bulk-passivated 3D sample, a perovskite film with MACl is considered as the control sample to specify the influence of the ThPyI passivator additive. Notably, more intense PL emission peaks are observed in the surface-passivated 3D/1D and bulk-passivated 3D perovskite films compared to the 3D control, shown in Figure 7a,b.

The high PL intensity is an indicator for the elimination of sub-bandgap states in perovskite films that are linked to defect states.[64] The emission peak of the surface-passivated

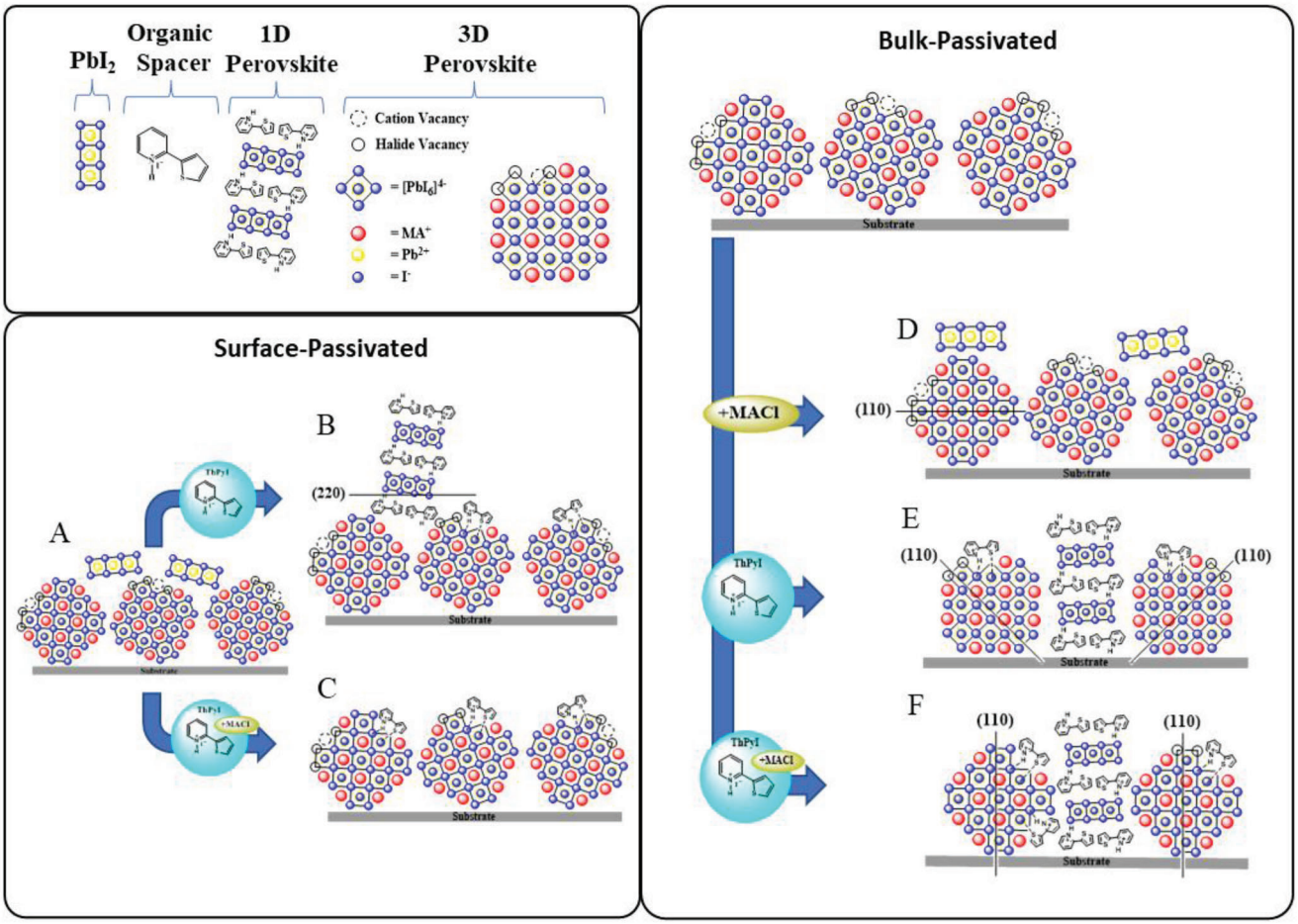

Figure 6. Schematic representation of crystal domain orientation in A) 3D MAPI control (with +5% excess PbI_2), B) ThPyI-surface-passivated 3D/1D, C) ThPyI-surface-passivated 3D/1D with MACl, D) 3D MAPI control with MACl, E) ThPyI-bulk-passivated 3D without MACl, and F) ThPyI-bulk-passivated 3D with MACl.

3D/1D perovskite is slightly blue shifted compared with the 3D control film in Figure 7a, which can be attributed to the 1D phase formed on top (Figure S13, Supporting Information). The emission peak of the bulk-passivated 3D perovskite appears at similar wavelength comparable with the 3D control with MACl as shown in Figure 7b.[64, 65]

The TRPL decay spectra of the corresponding films prepared on glass substrates are shown in Figure 7c,d. The TRPL curve was fitted using the following biexponential Equation (1):

$$y = A_1 \exp\left(\frac{-t}{\tau_1}\right) + A_2 \exp\left(\frac{-t}{\tau_2}\right) + y_0 \quad (1)$$

where A_1 and A_2 are the amplitudes. The symbols τ_1 and τ_2 express short and long charge carrier recombination times, respectively.[66] Here, we propose that τ_1 is related to the trap-assisted nonradiative recombination arising at the grain boundaries. On the other hand, τ_2 is associated with bulk carrier recombination.[67] The resulting charge carrier lifetimes of the perovskite films are listed (Table S5, Supporting Information).

In the 3D control film, the τ_1 and τ_2 values are equal to 50 and 114 ns, respectively. The values τ_1 and τ_2 of both bulk-passivated 3D and surface-passivated 3D/1D films are significantly extended compared to the control sample. The low τ_1 value indicates that the trap-assisted nonradiative recombination is reduced and radiative recombination of carriers dominates the PL decay in the bulk-passivated 3D and 3D/1D phases.[68]

The trap-state density of the corresponding films was quantified by the space-charge-limited current (SCLC) method for electron/hole-only devices, using the following Equation (2):

$$N_t = 2\varepsilon\varepsilon_0 V_{TFL}/qL^2 \quad (2)$$

where N_t is the trap-state density of electron or hole, ε is the relative dielectric constant of MAPI perovskite ($\varepsilon = 25$), ε_0 is vacuum permittivity (8.85×10^{-12} F m^{-1}), V_{TFL} is the trap-filled limit voltage, q is elementary charge (1.602×10^{-19} C) and L is the thickness of the perovskite film.[69] Electron-only devices were fabricated for this measurement and dark J–V curves were recorded (Figure S14, Supporting Information).

The linear region seen in the dark J–V curve at low bias voltage is the ohmic region. The intermediate bias region where the traps are filled with the charge carriers is known as the trap-filled region. The trap-free region is defined at the high-bias voltage.

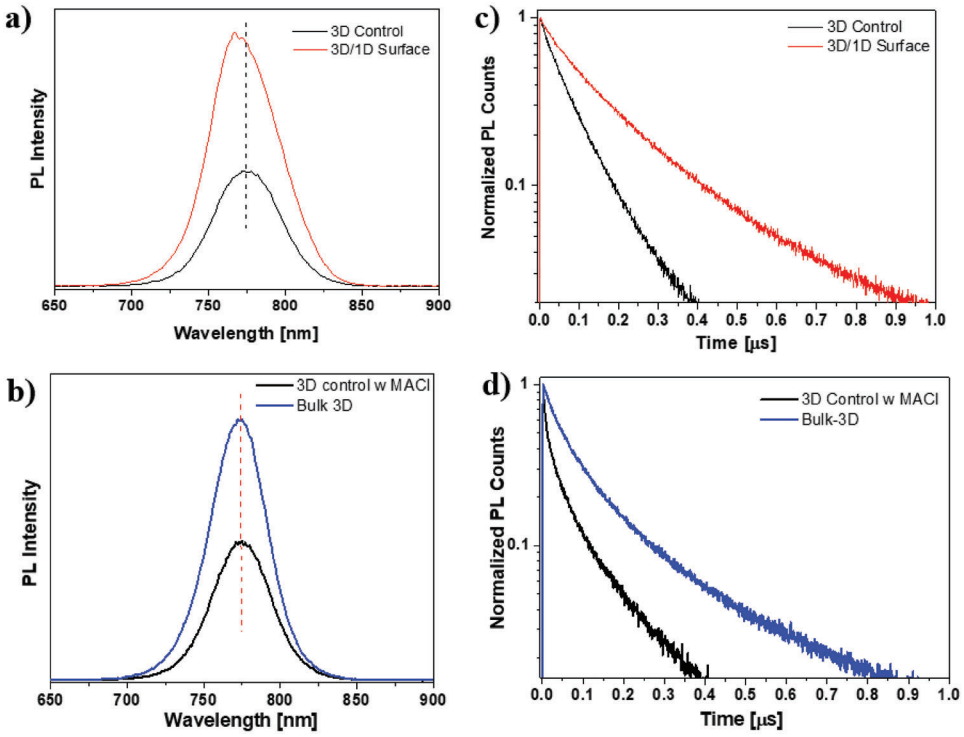

Figure 7. a,b) SSPL and TRPL spectra of 3D MAPI control and surface-passivated 3D/1D film, c,d) SSPL and TRPL spectra of 3D control with MACl and bulk-passivated 3D film.

The V_{TLF} is determined as the bias voltage at the inflection point between the ohmic region and the trap-filled region. The calculated trap state density of the 3D MAPI control device is 7.58×10^{15} cm^{-3}. For the surface-passivated 3D/1D device, the trap-state density is calculated to be 6.18×10^{15} cm $^{-3}$. The lower trap-state density in the surface-passivated 3D/1D perovskite device confirms that the low-dimensional 1D phase has a passivation effect and reduces the traps in the corresponding devices. In the case of bulk-passivated 3D perovskite the trap-state density was found to be 1.20×10^{16} cm^{-3}, and for the 3D MAPI control with the same device architecture it was found to be equal to 1.31×10^{16} cm^{-3}. These results suggest that in the bulk-passivated 3D film the ThPyI also acts as a passivator for the trap states, albeit with more moderate effect.

To evaluate further the effect of the 1D phase on the photovoltaic performance, the normal (*n-i-p*) planar perovskite solar cells for the 3D MAPI control, and the surface-passivated 3D/1D phases were fabricated as shown in **Figure 8**a. The device architecture of bulk-passivated 3D MAPI was kept inverted (*p-i-n*) because of the need for better energy alignment between the different layers given in Figure 8b.

As noted above, to increase the preferential orientation of perovskite slabs, MACl was used as an additive that plays an important role in improving the PCE of bulk-passivated 3D MAPI. Bulk-passivated 3D devices with and without MACl were fabricated for the purpose of comparison. Devices with the MACl/MAI 0.5 weight ratio show the highest performance (Figure S15, Supporting Information). The results of photovoltaic *J-V* characterization of the optimized devices, performed under AM 1.5G (1000 W m^{-2}), are presented in Figure 8c,d and Table S6, Supporting Information. Moreover, statistical distributions of the photovoltaic parameters are given (Figure S16, Supporting Information). The 3D MAPI control perovskite film yielded a short-circuit current density (J_{sc}) of 22.35 mA cm^{-2}, an open-circuit voltage (V_{oc}) of 1.09 V, and a fill factor (*FF*) of 74%, which gives an overall PCE equal to 18.08% (for the best performing device). As seen in the forward and backward scans, the 3D control device suffers from hysteresis. On the other hand, the surface-passivated

3D/1D device exhibits a higher PCE (19.60%) with improved V_{oc} of 1.11 V, J_{sc} of 22.69 mA cm^{-2}, and a FF of 78%. The improved V_{oc} suggests that the low-dimensional 1D phase grown at the grain boundaries of the 3D perovskite suppresses the trap-assisted recombination that is associated with surface defects. As for the optimized bulk-passivated 3D MAPI perovskite, the overall PCE was 14.10% with a J_{sc} of 18.98 mA cm^{-2}, V_{oc} of 1.02, and FF of 74% (For the best performing device). Hence, the efficiency of bulk-passivated 3D MAPI devices is lower than that of the surface-passivated 3D/1D perovskite device, presumably since it contains a high fraction of organic passivation agent (ThPyI: PbI_2; 2:3 mole ratio). We note that this is one of the first studies where 3D MAPI perovskite is prepared with a high volume fraction of organic agents in bulk-passivated perovskite solar cells.

The stability of the unencapsulated devices was studied under ambient conditions in air (room temperature, relative humidity 40–45%) as shown in Figure 8e. The surface-passivated 3D/1D perovskite device retained 85% of its PCE after a 1000 h stability test (under dark) whereas the PCE of the 3D control device dropped to 73% of its original PCE. On the other hand, the

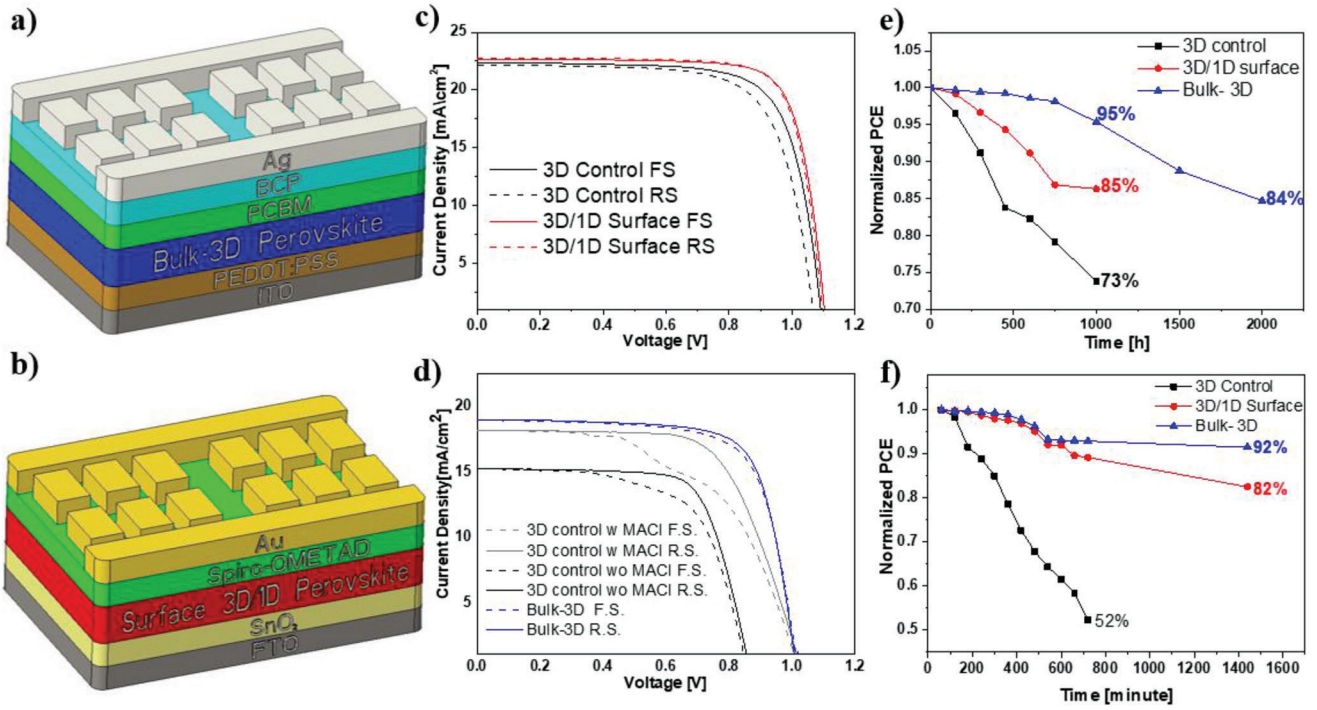

Figure 8. Device structure of a) bulk-passivated 3D and b) surface-passivated 3D/1D perovskite devices. c,d) *J–V* curves of surface-passivated 3D/1D and bulk-passivated 3D perovskite devices, e) long-term stability, and f) light-thermal stability of 3D control, surface-passivated 3D/1D, and bulk-passivated 3D devices.

bulk-passivated 3D perovskite device showed the best environmental stability among these devices, keeping 95.3% of its initial PCE after 1000 h, and 84% after 2000 h under N_2 atmosphere (dark). Furthermore, a combined light-thermal stability test of the corresponding devices was conducted under one sun at 60 °C for 24 h under N_2 atmosphere. The bulk-passivated 3D device also showed the highest light-thermal stability by retaining 92% of its initial efficiency under continuous light soaking after 24 h as shown in Figure 8f. In comparison, the initial PCE of surface-passivated 3D/1D and 3D MAPI control devices decreased to 82% and 52%, respectively. The improved stability of the surface-passivated 3D/1D device is attributed to the presence of the low-dimensional 1D phase, which is proposed to inhibit ion migration, moisture penetration, improve film quality, and reduce defects in the perovskite film. On the other hand, the high-volume fraction of hydrophobic ThPyI spacer used in the bulk-passivated 3D MAPI film should efficiently prevent moisture penetration, which apparently explains the higher stability. Remarkably, and in line with this assessment, the bulk-passivated 3D MAPI film retained its structure in air for 4 months after which time only a very weak diffraction peak of PbI_2 emerged (Figure S17, Supporting Information).

To find out the impact of the ThPyI-based low-dimensional new phase treatment on the hydrophobicity, the water contact angles of 3D $MAPbI_3$ control, 1D perovskitoid, surface-passivated 3D/1D, and bulk-passivated 3D perovskite films were measured. (Figure S18, Supporting Information). The pure 1D perovskitoid shows the highest water contact angle of around 73° compared to the others. As compared to the 3D $MAPbI_3$ control with an angle of 60°, the surface- and bulk-treated forms of the 3D perovskite films exhibit increased water contact angles of around 67° and 69°, respectively. The greater water contact angles of the 1D and treated 3D perovskite films compared to the 3D $MAPbI_3$ control reveal the enhanced hydrophobicity of the treated forms of the 3D perovskite.

The same films that were evaluated in the water contact angle measurements were immersed in water to further solidify their behavior in water. As expected, 3D control $MAPbI_3$ and its surface- and bulk-treated 3D films were decomposed into PbI_2 in a few seconds, which shows it with the characteristic yellow color of PbI_2. Interestingly, in the 1D film, no changes related to the color were observed. After removing the samples from the water and drying the corresponding films, XRD measurements were carried out to understand their behavior in water (Figure S19, Supporting Information). In comparison with the 3D control film and its treated forms, which show complete decomposition into PbI_2, the ThPyI-based low-dimensional pure new phase shows no decomposition. These water contact angle measurements and XRD diffractions of the water-immersed films show the water stability of the 1D phase compared with its 3D counterparts.

3. Conclusion

In summary, a novel thiophene based ThPyI organic spacer with heterocyclic structure was developed and used both as a defect passivator and as an organic spacer in surface- and bulk-passivated 3D MAPI-based perovskite devices. Our results demonstrate that the ThPyI organic spacer is a suitable candidate for creating 1D perovskitoids in perovskite-based photovoltaic devices. TRPL results showed that the fluorescence lifetimes in both

passivated devices become longer and contribute to the better performance. Moreover, the ThPyI based perovskite devices offered high efficiency and environmental stability compared to their 3D counterparts. The bulk-passivated 3D PV devices showed significantly higher environmental as well as light-thermal stability even compared to the surface-passivated devices. Importantly, this novel organic agent promoted the preferential orientation of the 3D perovskite slabs' crystalline orientation (vertical orientation of the (110) planes with respect to the substrate) in the films much more efficiently than the MACl additive. This study enriches the literature on thiophane-based organic spacers and presents a different perspective on organic spacer design. We envision that the above results can help to bring on a rational strategy for the design of organic agents that play a multiple role as defect passivator, crystalline orientation promoter, and organic spacer for various perovskite-based solar cells.

4. Experimental Section

Preparation of 3D MAPI Perovskite Precursor: The 3D control solution was prepared using PbI_2 (1.68 M, 5% excess), MAI (1.60 M), and DMSO (1.60 M) in 1 mL DMF.

Preparation of Bulk-Passivated 3D/1D Perovskite Precursor: The preparation of bulk-treated 3D/1D perovskite was prepared from the stoichiometric molar ratios of PbI_2, MAI, and Organic Spacer 3:2:2 in a 1 mL mixture of DMF:DMSO solvents (8:1 v/v). The weight ratio of MACl/MAI was equal to 0.5. The prepared solution for bulk-treated 3D/1D was stirred for 12 h at 70 °C.

Device Fabrication of 3D Control and Surface-Passivated 3D/1D Perovskite: Indium-tin-oxide (ITO) and fluorine-doped tin oxide (FTO) on glass substrates (3 × 3 cm) were etched using Zn powder and 3 M HCl for 5 min. Later, the ITO (or FTO) substrates were sonicated in 2% Hellmanex III cleaning solution (Sigma-Aldrich), double distilled water, ethanol, and isopropanol for 15 min in each medium, respectively. Afterward, the substrates were dried using nitrogen gas and subjected to nitrogen plasma at 50% power for 15 min. For the 3D MAPI control and the surface-passivated 3D/1D perovskite, a dilute water solution of SnO_2 nanoparticles (2.67 wt%) was spin-coated onto patterned FTO substrates in air at 4000 rpm for 35 s, and then annealed at 150 °C for 30 min. Before perovskite coating, SnO_2 coated FTO substrates were cleaned once again with nitrogen plasma for 10 min. Using the one-step "anti-solvent" method, the 3D MAPI perovskite precursor solution was deposited via spin-coating on top of the FTO/SnO_2 layer at 1000 rpm for 10 s, followed by 3500 rpm for 20 s. Ethyl acetate (400 µL) as an anti-solvent was dropped onto the perovskite film during the last 10 s of the spin coating step. The sample was then annealed at 130 °C for 10 min. For the surface treatment, the preheated (70°) 2-(thiophen-2-yl) pyridin-1-ium iodide salt (3.9 mg) with and without MACl/MAI (0.5) additive mixture in 1 mL isopropanol solution was spin-coated onto the perovskite films at 1000 rpm for 30 s followed by 5000 rpm for 5 s. Later, the samples were annealed at 100 °C for 10 min under N_2 atmosphere. The HTM was deposited by spin-coating (3000 rpm for 30 s) a solution of spiro-OMeTAD, which contain 72.3 mg spiro-OMeTAD, 35 µL *bis*(trifluoromethane) sulfonimide lithium salt (LiTFSI) stock solution (270 mg LiTFSI in 1 mL acetonitrile), 30 µL 4-*tert*-butylpyridine and 1 mL chlorobenzene. Finally, a 70 nm thin film of Au was thermally evaporated under high vacuum (1×10^{-6} Pa) on top of the hole transport layer.

Device Fabrication of Bulk-Passivated 3D MAPI: The PEDOT: PSS solution was spin-coated onto pre-cleaned ITO substrates at 2500 rpm for 40 s. The obtained ITO/PEDOT: PSS film was annealed at 140 °C for 20 min in air. Afterward, under inert atmosphere, the prepared perovskite solution was spin-coated onto the ITO/PEDOT: PSS substrate at 6000 rpm for 40 s, and toluene (350 µL) as an antisolvent was dropped onto the perovskite film during the last 15 s of the spin-coating process. Later, the film was annealed at 100 °C for 15 min. under N_2 atmosphere. After annealing the perovskite film, $PC_{61}BM$ (20 mg in 1 mL chlorobenzene) and bathocuproine (0.6 mg in 1 mL isopropanol) were spin-coated subsequently onto the perovskite active layer at 1000 rpm for 30 s respectively. After the last step, a 100 nm thick silver electrode was thermally evaporated under a vacuum of 1×10^{-6} Pa. The active area was defined using a metal mask with an area 0.0831 cm^2.

Details about the used materials, analytical methodologies, and synthesis of ThPyI and the 1D single crystals are presented in the Supporting Information.

Supporting Information

Supporting Information is available from the Wiley Online Library or from the author.

Acknowledgements

A.S. and A.B. contributed equally to this work. A.S. gratefully acknowledges the financial support of the Study Abroad Postgraduate Education Scholarship (YLSY) awarded by the Ministry of National Education, Republic of Turkey. The authors thank the Deutsche Forschungsgemeinschaft (DFG, German Research Foundation) under Germany's Excellence Strategy-EXC 2089/1-390776260 (e-conversion). T.A. acknowledges the financial support of the RSE International Joint Project (1787). S.E. acknowledges the financial support provided by the Slovenian Research Agency (N2-0221 and P2-0412). The authors also thank Dr. Marcus Frericks for Ultraviolet Photoelectron Spectroscopy (UPS).

Open access funding enabled and organized by Projekt DEAL.

Conflict of Interest

The authors declare no conflict of interest.

Data Availability Statement

Research data are not shared.

Keywords

1D perovskite, 3D/1D perovskite, bulk-passivated 3D perovskite, crystalline orientation promoter, passivation, solar cell

Received: February 2, 2023
Revised: April 30, 2023
Published online: May 25, 2023

[1] Q. Jiang, Y. Zhao, X. Zhang, X. Yang, Y. Chen, Z. Chu, Q. Ye, X. Li, Z. Yin, J. You, *Nat. Photonics* **2019**, *13*, 460.
[2] N. Torabi, A. Behjat, Y. Zhou, P. Docampo, R. J. Stoddard, H. Hillhouse, T. Ameri, *Mater. Today Energy* **2019**, *12*, 70.
[3] W. Zhang, G. E. Eperon, H. J. Snaith, *Nat. Energy* **2016**, *1*, 16048.
[4] G. Xing, N. Mathews, S. Sun, S. S. Lim, Y. M. Lam, M. Graïzel, S. Mhaisalkar, T. C. Sum, *Science* **2013**, *342*, 344.
[5] H. S. Kim, C. R. Lee, J. H. Im, K. B. Lee, T. Moehl, A. Marchioro, S. J. Moon, R. Humphry-Baker, J. H. Yum, J. E. Moser, M. Grätzel, N. G. Park, *Sci. Rep.* **2012**, *2*, 591.
[6] N. G. Park, M. Grätzel, T. Miyasaka, K. Zhu, K. Emery, *Nat. Energy* **2016**, *1*, 16152.

[7] X. Li, D. Bi, C. Yi, J. D. Décoppet, J. Luo, S. M. Zakeeruddin, A. Hagfeldt, M. Grätzel, *Science* **2016**, *353*, 58.
[8] S. de Wolf, J. Holovsky, S. J. Moon, P. Löper, B. Niesen, M. Ledinsky, F. J. Haug, J. H. Yum, C. Ballif, *J. Phys. Chem. Lett.* **2014**, *5*, 1035.
[9] C. C. Stoumpos, C. D. Malliakas, M. G. Kanatzidis, *Inorg. Chem.* **2013**, *52*, 9019.
[10] X. Li, M. I. Dar, C. Yi, J. Luo, M. Tschumi, S. M. Zakeeruddin, M. K. Nazeeruddin, H. Han, M. Grätzel, *Nat. Chem.* **2015**, *7*, 703.
[11] E. Khorshidi, B. Rezaei, D. Blätte, A. Buyruk, M. A. Reus, J. Hanisch, B. Böller, P. Müller-Buschbaum, T. Ameri, *Sol. RRL* **2022**, *6*, 2200023.
[12] E. Khorshidi, B. Rezaei, J. Hanisch, B. Böller, M. A. Reus, P. Müller-Buschbaumde, T. Ameri, *ACS Appl. Mater. Interfaces* **2022**, *14*, 54623.
[13] L. Wang, H. Zhou, J. Hu, B. Huang, M. Sun, B. Dong, G. Zheng, Y. Huang, Y. Chen, L. Li, Z. Xu, N. Li, Z. Liu, Q. Chen, L. D. Sun, C. H. Yan, *Science* **2019**, *363*, 265.
[14] C. Ortiz-Cervantes, P. Carmona-Monroy, D. Solis-Ibarra, *ChemSusChem* **2019**, *12*, 1560.
[15] C. Li, S. Tscheuschner, F. Paulus, P. E. Hopkinson, J. Kießling, A. Köhler, Y. Vaynzof, S. Huettner, *Adv. Mater.* **2016**, *28*, 2446.
[16] C. Eames, J. M. Frost, P. R. F. Barnes, B. C. O'regan, A. Walsch, M. F. Islam, *Nat. Commun.* **2015**, *6*, 7497.
[17] M. I. Saidaminov, J. Kim, A. Jain, R. Quintero-Bermudez, H. Tan, G. Long, F. Tan, A. Johnston, Y. Zhao, O. Voznyy, E. H. Sargent, *Nat. Energy* **2018**, *3*, 648.
[18] A. S. R. Bati, M. Batmunkh, J. G. Shapter, *Adv. Energy Mater.* **2020**, *10*, 1902253.
[19] H. Zhang, Y. Wu, C. Shen, E. Li, C. Yan, W. Zhang, H. Tian, L. Han, W. Zhu, *Adv. Energy Mater.* **2019**, *9*, 1803573.
[20] E. H. Jung, N. J. Jeon, E. Y. Park, C. S. Moon, T. J. Shin, T. Y. Yang, J. H. Noh, J. Seo, *Nature* **2019**, *567*, 511.
[21] E. Aydin, M. de Bastiani, S. de Wolf, *Adv. Mater.* **2019**, *31*, 1900428.
[22] F. Gao, Y. Zhao, X. Zhang, J. You, *Adv. Energy Mater.* **2020**, *10*, 1902650.
[23] Y. Huang, H. Luo, B. Zhang, K. Su, W. Chen, G. Sui, L. Liang, B. Zhang, J. Song, P. Gao, *Appl. Mater. Today* **2022**, *28*, 101550.
[24] A. Krishna, S. Gottis, M. K. Nazeeruddin, F. Sauvage, *Adv. Funct. Mater.* **2019**, *29*, 1806482.
[25] L. Mao, C. C. Stoumpos, M. G. Kanatzidis, *J. Am. Chem. Soc.* **2018**, *141*, 1171.
[26] H. Tsai, W. Nie, J. C. Blancon, C. C. Stoumpos, R. Asadpour, B. Harutyunyan, A. J. Neukirch, R. Verduzco, J. J. Crochet, S. Tretiak, L. Pedesseau, J. Even, M. A. Alam, G. Gupta, J. Lou, P. M. Ajayan, M. J. Bedzyk, M. G. Kanatzidis, A. D. Mohite, *Nature* **2016**, *536*, 312.
[27] J. Qian, Q. Guo, L. Liu, B. Xu, W. Tian, *J. Mater. Chem. A* **2017**, *5*, 16786.
[28] W. Fu, J. Wang, L. Zuo, K. Gao, F. Liu, D. S. Ginger, A. K. Y. Jen, *ACS Energy Lett.* **2018**, *3*, 2086.
[29] Y. Chen, Y. Sun, J. Peng, J. Tang, K. Zheng, Z. Liang, *Adv. Mater.* **2018**, *30*, 170348.
[30] J. Fan, Y. Ma, C. Zhang, C. Liu, W. Li, R. E. Schropp, Y. Mai, *Adv. Energy Mater.* **2018**, *8*, 1703421.
[31] P. Chen, Y. Bai, S. Wang, M. Lyu, J. Yun, L. Wang, *Adv. Funct. Mater.* **2018**, *28*, 1706923.
[32] C. C. Stoumpos, L. Mao, C. D. Malliakas, M. G. Kanatzidis, *Inorg. Chem.* **2017**, *56*, 56.
[33] D. Bi, P. Gao, R. Scopelliti, E. Oveisi, J. Luo, M. Grätzel, A. Hagfeldt, M. K. Nazeeruddin, *Adv. Mater.* **2016**, *28*, 2910.
[34] N. Yang, C. Zhu, Y. Chen, H. Zai, C. Wang, X. Wang, H. Wang, S. Ma, Z. Gao, X. Wang, J. Hong, Y. Bai, H. Zhou, B. B. Cui, Q. Chen, *Energy Environ. Sci.* **2020**, *13*, 4344.
[35] H. Lin, C. Zhou, Y. Tian, T. Siegrist, B. Ma, *ACS Energy Lett.* **2018**, *3*, 54.
[36] C. Zhou, Y. Tian, M. Wang, A. Rose, T. Besara, N. K. Doyle, Z. Yuan, J. C. Wang, R. Clark, Y. Hu, T. Siegrist, S. Lin, B. Ma, *Angew. Chem., Int. Ed.* **2017**, *56*, 9018.
[37] T. Kong, H. Xie, Y. Zhang, J. Song, Y. Li, L. Lim, A. Hagfeld, D. Bi, *Adv. Energy Mater* **2021**, *11*, 2101018.
[38] J. Im, C. C. Stoumpos, H. Jin, A. J. Freeman, M. G. Kanatzidis, *J. Phys. Chem. Lett.* **2015**, *6*, 3503.
[39] L. Gao, I. Spanopoulos, W. Ke, S. Huang, I. Hadar, L. Chen, X. Li, G. Yang, M. G. Kanatzidis, *ACS Energy Lett.* **2019**, *4*, 1763.
[40] P. Liu, Y. Xian, W. Yuan, Y. Long, K. Liu, N. U. Rahman, W. Li, J. Fan, *Adv. Energy Mater.* **2020**, *10*, 1903654.
[41] M. Pratheek, T. Abhinav, S. Bhattacharya, G. K. Chandra, P. Predeep, *Mater Sci. Technol.* **2021**, *4*, 282.
[42] S. Gharibzadeh, P. Fassl, I. M. Hossain, P. Rohrbeck, M. Frericks, M. Schmidt, T. Duong, M. R. Khan, T. Abzieher, B. A. Nejand, F. Schackmar, O. Almora, T. Feeney, R. Singh, D. Fuchs, U. Lemmer, J. P. Hofmann, S. A. L. Weber, U. W. Paetzold, *Energy Environ. Sci.* **2021**, *14*, 5875.
[43] G. Kim, H. Min, K. S. Lee, D. Y. Lee, S. M. Yoon, S. I. Seok, *Science* **2020**, *370*, 108.
[44] M. Jeong, I. W. Choi, E. M. Go, Y. Cho, M. Kim, B. Lee, S. Jeong, Y. Jo, H. W. Choi, J. Lee, J. H. Bae, S. K. Kwak, D. S. Kim, C. Yang, *Science* **2020**, *369*, 1615.
[45] C. Zhang, S. Wu, L. Tao, G. M. Arumugam, C. Liu, Z. Wang, S. Zhu, Y. Yang, J. Lin, X. Liu, R. E. I. Schropp, Y. Mai, *Adv. Energy Mater.* **2020**, *10*, 2002004.
[46] Z. Liu, F. Cao, M. Wang, M. Wang, L. Li, *Angew. Chem., Int. Ed.* **2020**, *59*, 4161.
[47] C. Ma, N. G. Park, *ACS Energy Lett.* **2020**, *5*, 3268.
[48] F. Li, X. Deng, F. Qi, Z. Li, D. Liu, D. Shen, M. Qin, S. Wu, F. Lin, S. H. Jang, J. Zhang, X. Lu, D. Lei, C. S. Lee, Z. Zhu, A. K. Y. Jen, *J. Am. Chem. Soc.* **2020**, *142*, 20134.
[49] L. Liu, S. Huang, Y. Lu, P. Liu, Y. Zhao, C. Shi, S. Zhang, J. Wu, H. Zhong, M. Sui, H. Zhou, H. Jin, Y. Li, Q. Chen, *Adv. Mater.* **2018**, *30*, 1800544.
[50] J. Peng, D. Walter, Y. Ren, M. Tebyetekerwa, Y. Wu, T. Duong, Q. Lin, J. Li, T. Lu, M. A. Mahmud, O. L. C. Lem, S. Zhao, W. Liu, Y. Liu, H. Shen, L. Li, F. Kremer, H. T. Nguyen, D. Y. Choi, K. J. Weber, K. R. Catchpole, T. P. White, *Science* **2021**, *371*, 390.
[51] X. Lin, D. Cui, X. Luo, C. Zhang, Q. Han, Y. Wang, L. Han, *Energy Environ. Sci.* **2020**, *13*, 3823.
[52] Y. Kuang, K. H. M. van der Werf, Z. S. Houweling, R. E. I. Schropp, *Appl. Phys. Lett.* **2011**, *98*, 113111.
[53] B. M. Kayes, H. A. Atwater, N. S. Lewis, *J. Appl. Phys.* **2005**, *97*, 114302.
[54] T. M. Koh, V. Shanmugam, J. Schlipf, L. Oesinghaus, P. Müller-Buschbaum, N. Ramakrishnan, V. Swamy, N. Mathews, P. P. Boix, S. G. Mhaisalkar, *Adv. Mater.* **2016**, *28*, 3653.
[55] C. Fei, L. Guo, B. Li, R. Zhang, H. Fu, J. Tian, G. Cao, *Nano Energy* **2016**, *27*, 17.
[56] A. Buyruk, D. Blätte, M. Günther, M. A. Scheel, N. F. Hartmann, M. Döblinger, A. Weis, A. Hartschuh, P. Müller-Buschbaum, T. Bein, T. Ameri, *ACS Appl. Mater. Interfaces* **2021**, *13*, 32894.
[57] H. Gökce, S. Bahceli, *Spectrochim. Acta, Part A* **2012**, *96*, 139.
[58] R. Szostak, J. C. Silva, S. H. Turren-Cruz, M. M. Soares, R. O. Freitas, A. Hagfeldt, H. C. N. Tolentino, A. F. Nogueira, *Sci. Adv.* **2019**, *5*, eaaw6619.
[59] M. A. Pérez-Osorio, Q. Lin, R. T. Phillips, R. L. Milot, L. M. Herz, M. B. Johnston, F. Giustino, *J. Phys. Chem. C* **2018**, *122*, 21703.
[60] H. Gökce, S. Bahceli, *J. Mol. Struct.* **2011**, *1005*, 100.
[61] W. S. Yang, B. W. Park, E. H. Jung, N. J. Jeon, Y. C. Kim, D. U. Lee, S. S. Shin, J. Seo, E. K. Kim, J. H. Noh, S. il Seok, *Science* **2017**, *356*, 1376.
[62] M. H. Li, H. H. Yeh, Y. H. Chiang, U. S. Jeng, C. J. Su, H. W. Shiu, Y. J. Hsu, N. Kosugi, T. Ohigashi, Y. A. Chen, P. S. Shen, P. Chen, T. F. Guo, *Adv. Mater.* **2018**, *30*, 1801401.

[63] M. Yavari, F. Ebadi, S. Meloni, Z. S. Wang, T. C. J. Yang, S. Sun, H. Schwartz, Z. Wang, B. Niesen, J. Durantini, P. Rieder, K. Tvingstedt, T. Buonassisi, W. C. H. Choy, A. Filippetti, T. Dittrich, S. Olthof, J. P. C. Baena, W. Tress, *J. Mat. Chem. A* **2019**, *7*, 23838.
[64] D. H. Cao, C. C. Stoumpos, O. K. Farha, J. T. Hupp, M. G. Kanatzidis, *J. Am. Chem. Soc.* **2015**, *137*, 7843.
[65] W. Wang, M. Cai, Y. Wu, K. Ji, B. Cheng, X. Liu, H. Lv, S. Dai, *Symmetry* **2022**, *14*, 1099.
[66] T. J. Jacobsson, J. P. Correa-Baena, E. Halvani Anaraki, B. Philippe, S. D. Stranks, M. E. F. Bouduban, W. Tress, K. Schenk, J. Teuscher, J. E. Moser, H. Rensmo, A. Hagfeldt, *J. Am. Chem. Soc.* **2016**, *138*, 10331.
[67] B. Wu, H. T. Nguyen, Z. Ku, G. Han, D. Giovanni, N. Mathews, H. J. Fan, T. C. Sum, *Adv. Energy Mater.* **2016**, *6*, 1600551.
[68] P. Chen, Y. Bai, S. Wang, M. Lyu, J. H. Yun, L. Wang, *Adv. Funct. Mater.* **2018**, *28*, 1706923.
[69] R. H. Bube, *J. Appl. Phys.* **2004**, *33*, 173.